Geochemistry Geophysics Geosystems G3

Published by AGU and the Geochemical Society

Article
Volume 12, Number 2
9 February 2011
Q02001, doi:10.1029/2010GC003404
ISSN: 1525-2027

Timing of magnetite formation in basaltic glass: Insights from synthetic analogs and relevance for geomagnetic paleointensity analyses

Julie A. Bowles
Institute for Rock Magnetism, Department of Geology and Geophysics, University of Minnesota, Twin Cities, Minneapolis, Minnesota 55455, USA (jbowles@umn.edu)

Jeffrey S. Gee
Scripps Institution of Oceanography, University of California, San Diego, La Jolla, California 92093, USA

Katherine Burgess and Reid F. Cooper
Department of Geological Sciences, Brown University, Providence, Rhode Island 02912, USA

[1] Absolute paleointensity estimates from submarine basaltic glass (SBG) typically are of high technical quality and accurately reflect the ambient field when known. SBG contains fine-grained, low-Ti magnetite, in contrast to the high-Ti magnetite in crystalline basalt, which has lead to uncertainty over the origin of the magnetite and its remanence in SBG. Because a thermal remanence is required for accurate paleointensity estimates, the timing and temperature of magnetite formation is crucial. To assess these factors, we generated a suite of synthetic glasses with variable oxygen fugacity, cooling rate, and FeO* content. Magnetic properties varied most strongly with crystallinity; less crystalline specimens are similar to natural SBG and have weaker magnetization, a greater superparamagnetic contribution, and higher unblocking temperatures than more crystalline specimens. Thellier-type paleointensity results recovered the correct field within 1σ error with 2 (out of 10) exceptions that likely result from an undetected change in the laboratory field. Unblocking and ordering temperature data demonstrate that low-Ti magnetite is a primary phase, formed when the glass initially quenched. Although prolonged heating at high temperatures (during paleointensity experiments) may result in minor alteration at temperatures < 580°C, this does not appear to impact the accuracy of the paleointensity estimate. Young SBG is therefore a suitable material for paleointensity studies.

Components: 11,300 words, 10 figures, 3 tables.

Keywords: submarine basaltic glass; paleointensity; magnetite.

Index Terms: 1519 Geomagnetism and Paleomagnetism: Magnetic mineralogy and petrology; 1521 Geomagnetism and Paleomagnetism: Paleointensity; 3630 Mineralogy and Petrology: Experimental mineralogy and petrology.

Received 19 October 2010; **Revised** 29 November 2010; **Accepted** 21 December 2010; **Published** 9 February 2011.

Bowles, J. A., J. S. Gee, K. Burgess, and R. F. Cooper (2011), Timing of magnetite formation in basaltic glass: Insights from synthetic analogs and relevance for geomagnetic paleointensity analyses, *Geochem. Geophys. Geosyst.*, *12*, Q02001, doi:10.1029/2010GC003404.

1. Introduction

[2] Submarine basaltic glass (SBG) has been increasingly used in recent years to recover geomagnetic paleointensity variations. A high percentage of specimens demonstrate ideal behavior in stepwise reheating experiments designed to recover paleointensity estimates, primarily because of the small grain size of the magnetite particles (compared to basalt) and because the glassy matrix may protect the particles against thermochemical alteration during the experiments. SBG has thus provided a new material for studying long-term fluctuations in geomagnetic intensity [e.g., *Selkin and Tauxe*, 2000; *Riisager et al.*, 2003; *Tauxe and Staudigel*, 2004; *Tauxe*, 2006]. Over shorter time scales where geomagnetic intensity fluctuations are independently known, glass paleointensities have been used to provide both absolute and relative age estimates of mid-ocean ridge lavas [e.g., *Gee et al.*, 2000; *Carlut and Kent*, 2000; *Carlut et al.*, 2004; *Bowles et al.*, 2005, 2006].

[3] SBG magnetization appears to be carried by low-Ti (titano)magnetite [*Pick and Tauxe*, 1994; *Carlut and Kent*, 2000], and it is the fine-grained nature of this magnetic carrier that makes it an ideal material for paleointensity experiments. To recover valid paleointensity estimates, however, the magnetic remanence carried by this phase must be a primary thermoremanent magnetization (TRM), i.e., the magnetization must be acquired at high temperatures when the glass initially cools. This premise has been questioned for SBG; *Heller et al.* [2002] argue [citing *Buddington and Lindsley*, 1964] that low-Ti magnetite is not an equilibrium phase in mafic lavas, which typically have titanomagnetite with ~60 mol percent ulvöspinel ($Fe_{2-x}Ti_xO_4$, with x = 0.6, or TM_{60}). Although equilibrium crystallization is not expected in quenched glass, *Heller et al.* [2002] suggested that SBG remanence is entirely chemical in origin and that it is acquired at ambient seafloor temperatures. If true, such an assertion would mean that paleofield estimates from SBG cannot provide a valid record of geomagnetic field intensity.

[4] A more plausible concern is that the magnetite crystallizes during cooling at elevated temperatures, but below the Curie or blocking temperature, thus acquiring a thermochemical remanent magnetization (TCRM) over part of the blocking temperature spectrum. In this case, only part of the blocking temperature spectrum may be legitimately used in recovering paleointensity. Because the origin of magnetite in SBG is not understood, a number of authors have expressed concerns over the validity of intensity estimates from glasses [e.g., *Smirnov and Tarduno*, 2003; *Morales et al.*, 2003; *Goguitchaichvili et al.*, 2004].

[5] We have therefore undertaken an experimental study designed to determine the conditions under which magnetite forms in basaltic glass and thereby to assess whether paleointensity determinations from SBG are valid. We explore the effects of temperature, melt composition, oxygen fugacity (fO_2), and cooling rate on the magnetic mineral assemblage in rapidly cooled basaltic melts. A companion study [*Burgess et al.*, 2010] additionally examines the possible role of posteruption oxidation in modification of the quenched glass. For comparison, we examine zero age, young (10s of kyr) and much older (up to ~100 Myr) natural samples. Finally, we present results from paleointensity experiments on synthetic samples generated in a known magnetic field to directly test the fidelity of the magnetic recording process.

2. Magnetic Remanence in Submarine Basaltic Glass

[6] Despite speculations (above) that SBG magnetization is a CRM acquired at ambient seafloor temperatures, there is abundant indirect evidence (summarized by *Tauxe and Staudigel* [2004] and *Bowles et al.* [2005]) suggesting that the low-Ti phase forms at high temperatures and carries predominantly a TRM. The strongest evidence supporting an original TRM in basaltic glass comes from analysis of historical flows where the geomagnetic field intensity is known. This straightforward test has been conducted in several localities. With one exception, in an area with extremely large local magnetic anomalies [*Carlut and Kent*, 2000], glass paleointensities from these historical flows give values consistent with the known field intensity [*Pick and Tauxe*, 1993b; *Mejia et al.*, 1996; *Carlut et al.*, 2000], including samples from a well-documented eruption at 9°50′N on the East Pacific Rise in 1991. A much larger number of samples (N = 26) presumed to be from the same flow were analyzed by *Bowles et al.* [2006]; again, the majority of results are consistent with the known field, although a few samples give paleointensity estimates lower than the expected field (with sample means up to 25% too low). Paleointensities from historical samples from the southern East Pacific Rise [*Bowles et al.*, 2005] also are consistent with

Table 1. Bulk Compositions of Starting Materials

	N10	N11	N14
SiO_2	49.94	50.57	51.32
TiO_2	1.73	1.99	2.58
Al_2O_3	14.83	14.12	13.70
FeO	10.11	11.27	13.69
MgO	7.71	6.82	5.82
MnO	0.18	0.21	0.22
CaO	11.75	11.14	10.71
Na_2O	2.95	2.98	2.25
K_2O	0.15	0.16	0.17
P_2O_5	0.18	0.19	0.20
Total	99.54	99.45	100.66

the known field, while paleointensities from older samples are consistent with all observational evidence of relative age, as well as limited radiometric ages determined by $^{210}Pb/^{226}Ra$ disequilibria [*Rubin et al.*, 2001; *Bergmanis et al.*, 2004].

[7] Many of the historical flows were sampled and measured within a few years or months of eruption. Therefore, if the magnetic remanence is acquired as magnetic minerals nucleate and grow after cooling, this must occur within a very short time (less than a few years). Seafloor alteration of basaltic glass begins with hydration, which results in the development of an amorphous gel-palagonite, enriched in Fe and Ti [*Stroncik and Schmincke*, 2001] and possibly containing amorphous Fe-Ti oxyhydroxides [*Kruber et al.*, 2008]. As hydration proceeds, the gel-palagonite eventually develops into crystalline clays, accompanied by authigenic precipitation of zeolites and other clays [*Muhe and Stoffers*, 1995; *Stroncik and Schmincke*, 2001; *Staudigel et al.*, 2008]. While this may include the weakly magnetic phase goethite, none of these processes result in the formation of magnetite or titanomagnetite. Furthermore, while these time scales are not well constrained, most young (<100 yr) submarine glasses show little to no evidence for palagonization or alteration.

[8] *Heller et al.* [2002] speculated that one way to quickly form magnetite in SBG at ambient seafloor temperatures is through a biomediated reaction. Young (<50 ka) glass may develop a biofilm encrusted in an Fe-rich precipitate [*Thorseth et al.*, 2001], and microbial alteration in 6 Ma basaltic glass was found to preferentially remove Fe (as well as Mg, Ca, and Na), replacing altered glass with phyllosilicates [*Alt and Mata*, 2000]. While these phyllosilicates may be enriched in Fe compared to abiotic alteration products [*Storrie-Lombardi and Fisk*, 2004], and secondary Fe sulfides have been associated with biotic alteration of glass [*Alt and Mata*, 2000; *Banerjee and Muehlenbachs*, 2003], there is no evidence to date suggesting microbial production of magnetite in SBG.

[9] Ambient seafloor alteration resulting in magnetite seems unlikely, but high-temperature, nonequilibrium crystallization processes may produce nonequilibrium (titano)magnetite. Thermodynamic calculations for a simple binary melt predict nonequilibrium compositions for rapid cooling [*Hort and Spohn*, 1991]. In an exploration of crystal nucleation in more complex, highly supercooled magnesium metasilicate melts, *Cooper et al.* [1991] induced the formation of metastable forsterite, despite the fact that it is not an equilibrium phase in the solid. They determined that this is achieved through a liquid-phase immiscibility that precedes crystallization. As a final example, *Zhou et al.* [2000] undertook a TEM study of a young (~5 yr) basalt pillow. They found that while slowly cooled titanomagnetite grains in the pillow interior have a near-equilibrium composition (~TM_{60}), smaller titanomagnetites in the rapidly cooled pillow margin have a much broader range in Ti content with an average (nonequilibrium) Ti/Fe ratio approaching that of the melt (~TM_{30}). This range in Ti content is consistent with the liquid phase separation process.

3. Methods

[10] The magnetic properties of synthetic glasses produced under controlled laboratory conditions allow evaluation of the conditions under which magnetite may be produced during vitrification. A set of synthetic basaltic glass samples was generated to evaluate the effect of variable cooling rate, fO_2, and composition (predominantly FeO* content) on the resulting magnetic mineralogy and to understand the magnetization of SBG.

3.1. Sample Selection and Synthesis

3.1.1. Synthetic Samples

[11] Crushed, natural basalts with three different bulk compositions (10, 11, and 14 wt% FeO*; Table 1) were melted in alumina crucibles at 1400°C for 2 h in a vertically oriented, gas-mixing furnace (Figure 1). Temperature was then reduced over 2 h to 1210°C, or 10°C to 40°C above the liquidus as calculated using the MELTS algorithm [*Ghiorso and Sack*, 1995]. The samples were equilibrated at 1210°C for 3 h before cooling. fO_2 was controlled via flowing CO-CO_2 (with the appropriate mixture calculated for 1210°C) and was varied about the

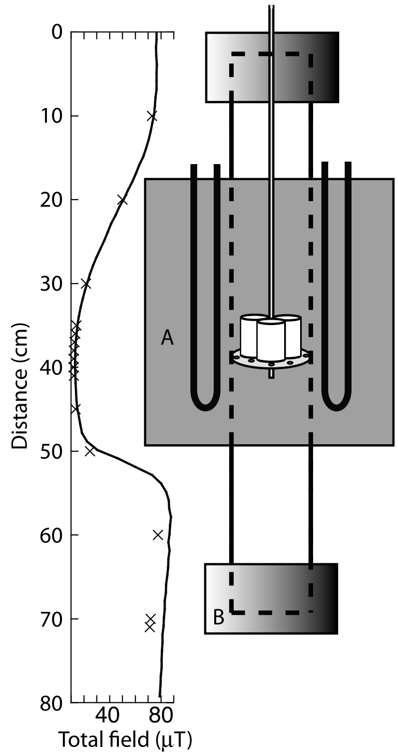

Figure 1. Schematic drawing of experimental setup for glass synthesis (only vertical axis to scale, and crucibles in reality are 3 cm tall). A Deltech Model DT/31/VT05/EMS furnace is equipped with a 2 in. inner diameter alumina tube (dashed-solid line). A gas-tight seal is provided by O-rings cooled by aluminum water jackets at the top and bottom of the tube. $MoSi_2$ heating elements (heavy, solid lines) are housed inside a steel box that is lined with ceramic insulation. Three sample crucibles (one for each composition) are placed on an alumina disc attached to a rod that can slide up and down. A thermocouple is threaded through the rod with the junction located between the three crucibles. Samples cooled through their blocking temperature (with elements off) are at either position A (field ~13 μT) or B (field ~80 or ~72 μT; see text). The field measured prior to (solid line) and after (crosses) experiments is given at left.

quartz-fayalite-magnetite (QFM) buffer by $\pm 1 \log_{10}$ unit (QFM − 1 to QFM + 1). One second temperature measurements during cooling allowed estimation of cooling rates. Actual sample cooling rates are likely somewhat slower, especially for the most rapidly cooled samples, as a result of the large thermal mass of the crucible and sample. Cooling rate at 1000°C (approximate temperature of peak oxide formation) was varied by approximately an order of magnitude from ~16°C min^{-1} to ~150°C min^{-1}. This was accomplished in one of the following three ways. (1) For the most rapidly cooled samples, the samples were quickly (<10 s) lowered to the bottom of the furnace tube (position B; Figure 1), which extends below the furnace box. (2) Samples cooled at an intermediate rate were slowly lowered to the bottom of the furnace tube, trying to maintain a cooling rate of ~70°C min^{-1} near 1000°C; however, the actual rate varied between ~60°C min^{-1} and 95°C min^{-1} between 1200°C and 800°C. (3) Samples cooled "slowly" were allowed to cool in the center of the furnace (position A; Figure 1). In all cases samples were stationary well before passing through the Curie temperature of magnetite (580°C), and power to the furnace elements was shut off immediately prior to cooling. Samples were all cooled in (controlled-atmosphere) air, as opposed to water quenching (see section 5.1). Experimental conditions are summarized in Table 2.

[12] Samples cooled in the ambient laboratory field, which varied considerably with vertical position relative to the furnace and the enclosing metal box. The vertical field gradient was measured before and after the complete set of sample syntheses; while the field in the center of the furnace remained relatively stable (position A; Figure 1), that near the bottom (position B; Figure 1) was more subject to temporal variations and is less well constrained. Slowly cooled samples cooled in the center of the furnace (position A; Figure 1) in a relatively low field (~13 μT), while rapidly cooled samples cooled near the bottom (position B; Figure 1) in a relatively high field (~72 or ~80 μT). Following sample synthesis, the natural remanent magnetization (NRM) of the samples was measured prior to subsectioning. Samples were then sectioned longitudinally into thirds; one third was used for petrographic analyses, the center third was further subdivided for rock magnetic and paleointensity experiments, and the final third was reserved as an archive. When preparing subsamples (specimens) for magnetic analyses, care was taken to note the approximate relative position with respect to the crucible wall whenever possible. Specimens were thus placed into three groups: mostly glassy centers (designated group A), specimens directly adjacent to or in contact with the crucible wall (group C), and specimens from some intermediate position (group B).

3.1.2. Natural Samples

[13] A set of natural SBG was selected for comparison of magnetic properties against the synthetic samples. The natural samples span a range of ages and magnetization intensities. The latter was intended as a proxy for varying degrees of crystallinity, as

Table 2. Experimental Conditions for Sample Synthesis

Experiment	Sample ID[a]	Approximate Cooling Rate (°C min^{-1}) 1000°C	Approximate Cooling Rate (°C min^{-1}) 700°C	fO_2 ΔQFM	Approximate Field (μT)
7	M-Nxx-7	153	80	−1	72
4	M-Nxx-4	150[b]	80[b]	0	80
2	M-Nxx-2	162	81	0.5	80
5	M-Nxx-5	149	75	1	80
8	M-Nxx-8	68	34	0	72
11	M-Nxx-11	16	5.4	−1	13
3	M-Nxx-3	16[b]	5.5[b]	0	13
6	M-Nxx-6	16	5.5	1	13

[a] Each sample is the contents of a single crucible. Here xx is either 10, 11, or 14, denoting approximate FeO* content. The final number denotes sequential experiment number; all samples synthesized at the same time share an experiment number.

[b] Cooling rates are not measured directly, but they are estimated based on measurements made under similar conditions.

magnetization generally increases with depth into the glassy margin. The youngest samples (typically ≤40 ka) were collected via submersible near the axis of the Northern East Pacific Rise. Samples dredged from the flanks of the Southern East Pacific Rise are ~200 ka, and a set of Cretaceous (~92 Ma) glass was collected from the Troodos ophiolite [*Tauxe and Staudigel*, 2004].

3.2. Rock Magnetic Experiments

[14] In addition to the natural samples, four synthetic specimens from each crucible were selected for rock magnetic analyses, encompassing the observed range of crystallinity and magnetization within the crucible. Magnetization (M) versus applied field (B) data (M versus B) were acquired on all specimens at room temperature to a maximum field of (typically) 1 T. Low-temperature cycling (300 K → 10 K → 300 K) of a room temperature saturation (2.5 T) isothermal remanence (SIRM) was carried out on a subset of specimens. (Other low-temperature data were not diagnostic, but are given in the auxiliary material.)[1] Continuous thermomagnetic measurements typically used to derive Curie temperatures were hampered by the extremely low ferromagnetic to paramagnetic ratio in most specimens. For two specimens, we therefore measured magnetic hysteresis as a function of temperature up to 600°C to derive the temperature dependence of saturation magnetization. For the remainder of the specimens, we determined unblocking temperature spectra via thermal demagnetization of a 2.5 T IRM. Finally, to test for possible magnetite growth on time scales relevant to paleointensity experiments we gave a 1.5 T IRM to 6 natural glass specimens with varying chemistries and of estimated ages ranging from ~10–1000 yr. The specimens were then heated to 100°C and held at this temperature for 1 h. After cooling, the specimens were again given an IRM and measured. This process was repeated at 100°C, and then at successively higher temperatures, so that the specimens spent a total of 2 h at each temperature.

3.3. Paleointensity Experiments

[15] Five to eight additional specimens from each crucible were selected for Thellier-type [*Thellier and Thellier*, 1959] paleointensity experiments, again taking care to encompass the range of magnetization present within the crucible. A significant number of the glassiest samples, however, had NRM moments too low to accurately measure as thermal demagnetization proceeded ($<10^{-10}$ Am^2). Glass chips were immobilized in glass tubes that had been previously screened for low TRM acquisition ($<3 \times 10^{-11}$ Am^2). We used the IZZI protocol [*Yu et al.*, 2004; *Yu and Tauxe*, 2005], which alternates the order in which the in-field and zero-field treatments are applied. Treatments were spaced at 25°C intervals from 100°C to 550°C, and pTRM checks [*Coe*, 1967] were carried out every 50°C during the 'ZI' steps (zero-field followed by in-field cooling). A laboratory field of 20, 40, or 75 μT was used for the in-field steps (Table 3).

[16] Anisotropy of thermal remanent magnetization (ATRM) was evaluated for all specimens that resulted in successful paleointensity interpretations (see below). Specimens were first demagnetized at 25°C above the highest temperature used for the Thellier experiment and then subsequently given a total TRM at the highest temperature used in the Thellier experiment (350°C, 450°C or 550°C), along the specimen +X, +Y, +Z and −X, −Y, −Z directions.

---

[1] Auxiliary materials are available in the HTML. doi:10.1029/2010GC003404.

Table 3. Paleointensity Results[a]

Sample ID	Spec ID	Type	NRM ($Am^2 kg^{-1}$)	Npts	Low	High	f	g	q	$\sigma_b/\lvert b \rvert$	MAD	DANG	DRAT	Blab	Buncor	Bcor
M-N10-2	a5b	B	2.42E-04	8	125	300	0.85	0.84	13.2	0.054	0.9	1.1	5.0	40	83.3	82.9
M-N10-2	a5c	A	3.23E-06	13	125	425	0.87	0.90	13.5	0.058	3.2	2.1	6.4	40	80.1	83.9
M-N10-2	a5e	B	1.02E-04	10	125	350	0.87	0.86	25.4	0.029	1.1	0.6	2.7	40	89.9	88.8
M-N11-2	a2.2c	C	7.03E-05	12	0	350	0.92	0.87	35.1	0.023	2.2	2.1	4.7	40	78.9	73.0
M-N11-2	a2.2d	C	1.37E-05	12	0	350	0.94	0.89	14.6	0.057	2.3	0.7	4.6	40	82.0	72.3
M-N11-2	a3.2b	C	2.67E-05	7	200	350	0.52	0.82	13.6	0.031	5.9	5.6	7.0	40	62.8	82.4
M-N14-2	a1a	A	2.88E-06	12	0	350	1.00	0.87	42.8	0.020	0.8	0.5	1.9	40	73.0	72.6
M-N14-2	a5a	A	1.10E-05	10	125	350	0.92	0.86	86.8	0.009	1.7	1.2	1.3	40	51.8	75.0
M-N14-2	a5c	B	9.18E-05	10	0	300	0.93	0.85	46.5	0.017	1.5	1.0	1.3	40	87.7	72.3
M-N14-2	a5d	B	1.30E-04	8	125	300	0.91	0.83	14.9	0.051	1.9	0.1	3.1	40	63.5	71.8
M-N14-2	a5e	B	1.98E-04	9	100	300	0.89	0.84	28.9	0.026	1.7	1.2	4.3	40	78.3	77.1
M-N14-2	a5f	B	7.22E-06	10	125	350	0.97	0.86	48.1	0.017	0.8	0.3	0.9	40	70.6	74.4
Average															75.2	77.2
SD															11.3	5.8
M-N10-3	a1a	A	6.22E-07	15	0	400	0.88	0.90	17.1	0.047	11.5	13.2	4.6	20	7.9	9.8
M-N10-3	a3.1	B	1.98E-06	15	125	450	0.83	0.90	16.9	0.044	8.2	3.8	5.6	20	17.6	15.4
M-N11-3	a4b	C	7.31E-04	11	0	300	0.99	0.79	14.6	0.053	1.7	0.8	5.8	20	12.0	11.7
Average															12.5	12.3
SD															4.9	2.8
M-N10-4	a4a	C	1.67E-05	17	0	450	0.90	0.90	36.8	0.022	4.0	3.2	5.7	75	86.6	85.5
M-N10-4	a4b	C	2.90E-05	14	0	375	0.86	0.89	37.6	0.020	1.7	0.7	4.8	75	86.0	87.0
M-N11-4	2.2a	C	6.94E-05	11	0	300	0.88	0.84	23.2	0.032	1.9	2.6	4.9	75	74.2	72.2
M-N11-4	a4b	C	1.32E-04	12	0	325	0.88	0.87	23.0	0.033	1.7	1.7	4.5	75	83.0	84.4
M-N14-4	a3.2c	C	1.50E-05	11	0	300	0.94	0.87	14.6	0.056	5.5	4.6	2.9	75	90.1	81.1
M-N14-4	a4.1a	B	1.63E-05	11	0	300	1.01	0.84	26.0	0.032	2.5	1.0	5.7	75	62.7	72.9
Average															80.4	80.5
SD															10.2	6.5
M-N10-5	a2b	B	9.81E-07	13	175	450	0.90	0.87	32.5	0.024	6.6	1.0	5.0	75	62.3	68.8
M-N10-5	a3.2b2	C	1.05E-04	9	150	325	0.77	0.84	27.4	0.024	1.9	1.5	6.6	75	70.7	73.4
M-N10-5	a4a	C	5.07E-05	10	125	325	0.80	0.86	34.8	0.020	2.0	2.5	4.3	75	93.2	91.1
M-N11-5	a2.1a	B	3.76E-06	11	175	400	0.85	0.85	78.3	0.009	3.1	2.3	3.1	75	85.1	77.5
M-N11-5	a2.2b	C	2.31E-05	13	0	350	0.95	0.90	36.5	0.023	4.9	1.2	2.4	75	94.7	78.0
M-N11-5	a3.1d	C	7.51E-05	12	0	325	0.90	0.88	31.8	0.025	2.7	1.4	4.4	75	86.6	79.2
M-N11-5	a5e	B	7.88E-05	11	150	375	0.87	0.86	70.3	0.011	2.8	1.2	2.5	75	82.8	105.0
M-N14-5	a1b1	C	4.66E-04	11	0	300	0.90	0.87	18.2	0.043	1.7	0.9	3.9	75	85.2	82.1
M-N14-5	a4.1d	C	1.97E-03	10	0	275	0.94	0.85	14.1	0.057	2.0	0.8	1.7	75	113.6	84.4
Average															86.0	82.2
SD															14.6	10.7
M-N10-6	a2.2a1	C	4.93E-04	13	100	375	0.82	0.87	17.6	0.041	3.5	2.9	5.4	20	12.9	14.0
M-N10-6	a2.2a4	C	1.05E-03	13	0	350	0.92	0.84	17.3	0.044	2.6	4.3	6.3	20	13.3	14.0
M-N10-6	a3.1d	B	5.07E-06	14	100	400	0.84	0.91	25.6	0.030	5.9	3.6	5.8	20	24.7	22.3
M-N10-6	a4c	C	7.15E-04	11	0	300	0.87	0.84	28.2	0.026	2.4	2.5	6.7	20	13.3	12.6
M-N11-6	a2.2a	C	1.52E-04	14	0	375	0.95	0.88	32.8	0.025	4.3	1.2	4.3	20	16.6	19.3
M-N11-6	a2.2f	C	1.35E-03	12	100	350	0.76	0.84	14.0	0.045	2.9	3.2	6.1	20	15.7	15.0
M-N11-6	a2.2h	C	1.25E-03	15	0	400	0.87	0.90	22.6	0.035	2.2	1.3	5.5	20	11.5	13.0
M-N11-6	a3.2a	C	7.53E-04	13	0	350	0.91	0.87	24.5	0.032	3.2	4.1	5.5	20	12.0	14.4
M-N11-6	a3.2d	C	7.29E-05	15	0	400	0.97	0.89	22.3	0.039	3.4	1.9	5.7	20	47.0	13.5
M-N11-6	a4c	B	2.26E-03	13	0	350	0.92	0.86	20.8	0.038	3.1	3.2	4.9	20	14.1	16.1
M-N14-6	a2.2a	C	4.85E-04	7	0	200	0.98	0.70	11.8	0.058	2.2	0.9	5.5	20	13.5	13.0
Average															17.7	15.2
SD															10.4	3.0
M-N10-7	a2.2a1	C	7.91E-06	13	0	350	0.56	0.90	29.2	0.017	4.4	4.2	2.0	75	60.3	60.5
M-N11-7	a2.1a	B	1.07E-06	15	0	400	0.88	0.90	24.6	0.032	6.3	2.8	6.6	75	51.8	49.8
M-N11-7	a3.1a	B	5.96E-06	15	0	400	0.88	0.91	41.2	0.019	1.6	0.3	3.4	75	62.4	63.3
M-N11-7	a3.2b	C	3.04E-05	17	0	450	0.93	0.91	27.4	0.031	1.6	0.3	3.7	75	49.4	55.1
M-N11-7	a3.2h	C	9.53E-05	14	0	375	0.90	0.89	29.0	0.027	2.1	2.3	3.8	75	58.8	62.6

Table 3. (continued)

Sample ID	Spec ID	Type	NRM ($Am^2\ kg^{-1}$)	Npts	Low	High	f	g	q	σ_b/|b|	MAD	DANG	DRAT	Blab	Buncor	Bcor
M-N14-7	a2.2c	C	6.11E-05	12	0	325	0.92	0.85	32.6	0.024	1.8	1.6	5.8	75	66.9	66.9
M-N14-7	a3.1c	C	1.37E-04	12	0	325	0.88	0.87	29.4	0.026	2.4	2.5	6.1	75	62.7	68.1
M-N14-7	a3.2b	C	2.21E-06	12	0	325	0.90	0.82	24.4	0.030	5.8	1.5	5.3	75	57.6	61.3
M-N14-7	a4.1	B	7.99E-06	12	0	325	0.86	0.88	34.9	0.022	2.2	1.6	6.3	75	69.0	61.8
Average															59.9	61.0
SD															6.4	5.6
M-N10-8	a2.1c	C	6.83E-05	15	0	400	0.78	0.92	59.9	0.012	1.9	1.6	2.9	75	70.4	70.5
M-N10-8	a2.2a1	C	1.15E-04	11	0	300	0.73	0.87	16.1	0.040	2.3	3.6	2.9	75	68.7	68.8
M-N10-8	a3.1c	C	8.42E-05	14	100	400	0.76	0.91	28.8	0.024	2.9	2.3	4.0	75	74.2	75.5
M-N10-8	a3.2a2	C	1.83E-04	14	100	400	0.69	0.89	24.5	0.025	2.2	1.5	3.2	75	61.8	63.6
M-N10-8	a4b	C	7.91E-05	16	0	425	0.87	0.92	61.7	0.013	3.5	5.2	3.3	75	66.1	69.6
M-N11-8	a2.1a	B	1.10E-06	12	0	325	0.92	0.89	20.9	0.039	5.5	4.2	4.3	75	65.8	66.9
M-N11-8	a2.1c	B	2.89E-04	15	0	400	0.89	0.90	39.9	0.020	3.0	1.9	4.9	75	51.3	59.0
M-N11-8	a3.1a	B	1.77E-06	11	0	300	0.86	0.85	22.2	0.033	6.1	14.3	3.2	75	58.8	55.4
M-N11-8	a3.2a	B	3.37E-05	17	0	450	1.01	0.89	34.3	0.026	3.6	3.0	3.5	75	57.0	53.3
M-N11-8	a4d	C	2.86E-04	17	0	450	0.93	0.90	29.2	0.029	1.2	0.2	4.1	75	66.5	66.9
M-N14-8	a3.1a	B	4.11E-04	9	0	250	0.90	0.80	17.0	0.042	1.8	0.7	5.7	75	68.6	61.1
M-N14-8	a3.1d	B	2.12E-05	11	0	300	0.94	0.83	22.1	0.035	1.5	0.4	3.8	75	81.5	57.3
Average															65.9	64.0
SD															8.0	6.8
M-N10-11	a2.2a	B	4.10E-05	14	0	400	0.95	0.84	14.7	0.054	6.1	2.1	5.2	40	15.3	14.7
M-N10-11	a3.2a	C	7.66E-05	10	0	300	0.84	0.81	13.3	0.051	7.8	3.4	5.7	40	12.9	12.8
M-N11-11	a2.2c	C	3.00E-04	11	100	350	0.67	0.85	29.6	0.019	6.6	12.1	5.2	40	12.1	14.4
M-N11-11	a4a	C	1.65E-04	12	0	350	0.98	0.85	23.2	0.036	1.8	3.2	4.0	40	11.9	11.9
M-N11-11	a4c	C	2.31E-04	12	0	350	0.96	0.84	29.2	0.028	3.0	4.5	4.3	40	11.5	11.8
M-N14-11	a2.2a	C	6.61E-05	8	0	250	0.96	0.68	19.8	0.033	6.2	2.4	5.3	40	8.1	10.7
M-N14-11	a3.2a	C	2.11E-05	7	100	250	0.54	0.76	9.6	0.043	6.4	5.3	6.4	40	9.4	12.1
M-N14-11	a4b	C	1.30E-04	7	0	225	0.93	0.70	25.9	0.025	3.9	4.0	5.9	40	12.4	11.2
M-N14-11	a4c	C	2.93E-04	7	0	225	0.94	0.75	17.5	0.040	3.4	6.1	6.3	40	12.3	12.9
Average															11.8	12.5
SD															2.1	1.4

[a] Paleointensity results listed only for specimens passing quality selection criteria (see text). Sample ID, see Table 2 for synthesis conditions linked to Sample ID; SD, standard deviation. Spec ID, specimen ID. Type is approximate position of specimen with respect to crucible wall: A, crucible center; C, adjacent to crucible wall. Npts, number of points used in paleointensity determination; Low, lowest temperature (°C) used in paleointensity determination; High, highest temperature (°C) used in paleointensity determination; f, fraction of NRM used in paleointensity determination [*Coe et al.*, 1978]; g, gap factor [*Coe et al.*, 1978]; q, quality factor [*Coe et al.*, 1978]; σ_b/|b|, standard error of the slope divided by slope [*Coe et al.*, 1978]; MAD, maximum angular deviation [*Kirschvink*, 1980]; DANG, deviation angle [*Tauxe and Staudigel*, 2004]; DRAT, maximum difference ratio [*Selkin and Tauxe*, 2000]; Blab, lab field used during paleointensity experiments (μT); Buncor, paleofield prior to TRM anisotropy correction (μT); Bcor, paleofield after TRM anisotropy correction (μT).

A third set of total TRMs along the +X, +Y, +Z directions was used to monitor any mineralogical changes and to evaluate reproducibility.

4. Results

4.1. Microscopy

[17] All quenched synthetic samples vary in crystallinity from sample center to the crucible edge. Under an optical microscope, samples were glassy with few to no visible crystals in the crucible center, while portions in contact with the crucible were relatively more crystalline, resulting from heterogeneous nucleation on the crucible wall and perhaps enhanced by alumina contamination. A zone of elongate plagioclase crystals and sparse oxide crystals adjacent to the crucible wall transitions to a spherulitic zone and then to glass in slowly cooled (16°C min^{-1}) samples (Figure 2a). We use the term "spherulitic" to refer to fine intergrowths of plagioclase and pyroxene, which in natural samples are frequently centered about a plagioclase microlite [e.g., *Marescotti et al.*, 2000]; the term should not be confused with that used to describe spherical clusters of blade-like, radiating crystals frequently found in rhyolitic glass, that often result from devitrification [e.g., *Lofgren*, 1971]. The largest oxide minerals near the crucible wall are typically 1–3 μm in diameter, which would correspond to a multidomain or pseudo-single-domain state in magnetite. In quickly cooled samples, no oxides are visible and a continuous spherulitic zone is absent, although small, discontinuous spher-

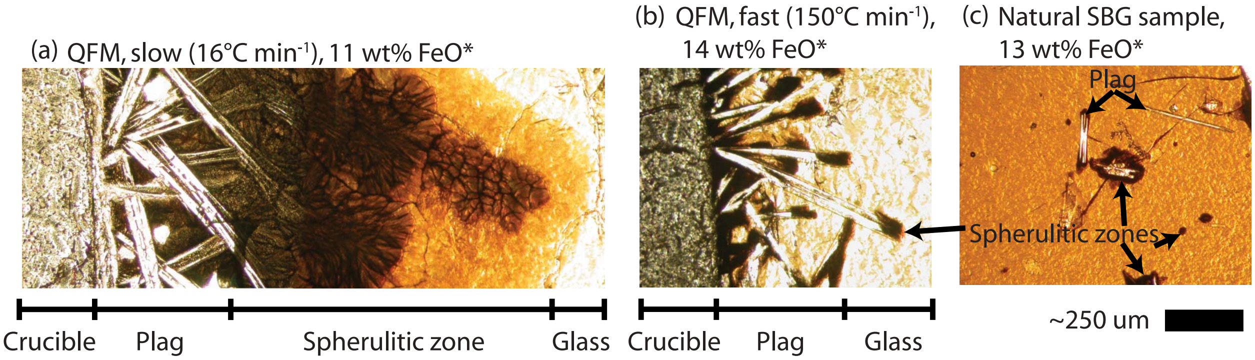

Figure 2. Transmitted light images of representative samples. Most synthetic samples were relatively glassy with few to no visible crystals in the center of the crucible, while portions in contact with the crucible were relatively more crystalline. (a) A zone of plagioclase adjacent to the crucible wall transitions to a spherulitic zone and then glass in slowly cooled samples. (b) In quickly cooled samples a continuous spherulitic zone is absent, though small spherulitic regions are found at the tips of plagioclase crystals. (c) A natural sample has similar features, including elongate plagioclase grains, often surrounded by spherulitic zones. Plag, plagioclase. Scale bar is the same for Figures 2a–2c.

ulitic areas are associated with the ends of the plagioclase crystals (Figure 2b). At a ~30 nm scale, glass generated in a companion experiment [*Burgess et al.*, 2010] is completely uniform away from the crucible walls. However, in high-magnification TEM amorphous immiscibility and (very sparse) nanocrystals are present [*Burgess et al.*, 2010, Figure 2]. Diffraction patterns are not indexable, but indicate a cubic phase.

[18] Natural samples all have some plagioclase crystals present (Figure 2c), as well as spherulitic zones, suggesting some affinity with the slightly crystalline portions of the synthetic samples. The spherulitic zones can be seen either at the ends of or wholly encasing the plagioclase phenocrysts (Figure 2c) and result from undercooling [*Kirkpatrick*, 1978].

4.2. Rock Magnetic Results

4.2.1. Remanence Data

[19] NRM of the bulk synthetic samples (prior to sectioning) varies by more than two orders of magnitude (Figure 3). As expected, NRM is positively correlated with fO_2 and negatively correlated with cooling rate, presumably reflecting relative variations in the concentration of oxide minerals. The samples with 10 wt% FeO* have, with one exception, lower magnetization than those with 11 wt% FeO*. NRMs of the 14 wt% FeO* samples are roughly equivalent to those of the 11 wt% FeO* samples, typically slightly higher at fast cooling rates and somewhat lower at slow cooling rates (Figure 3), indicating that factors other than bulk Fe content affect nucleation and growth of Fe oxides. When subdivided, NRM within the crucible (measured on individual specimens) varies by up to four orders of magnitude with considerable heterogeneity, but is always lowest in the glassy center, at or below the magnetometer measurement threshold (~3×10^{-11} Am^2). This is similar to natural SBG, where the lower limit to NRM is at or below the measurement threshold, and NRM varies over two to three orders of magnitude.

4.2.2. Magnetization Versus Applied Field (Hysteresis) Data

[20] Most group A and group B synthetic samples were dominated by a paramagnetic signal (e.g., Figure 4a), while group C samples (those closest to

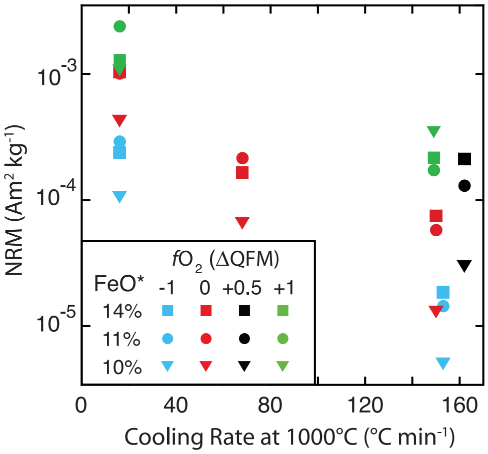

Figure 3. NRM (normalized to a 35 μT applied field) of bulk samples prior to subsampling. When subdivided, specimen magnetization within the crucible varies by up to four orders of magnitude with considerable heterogeneity, but is always lowest in the glassy center.

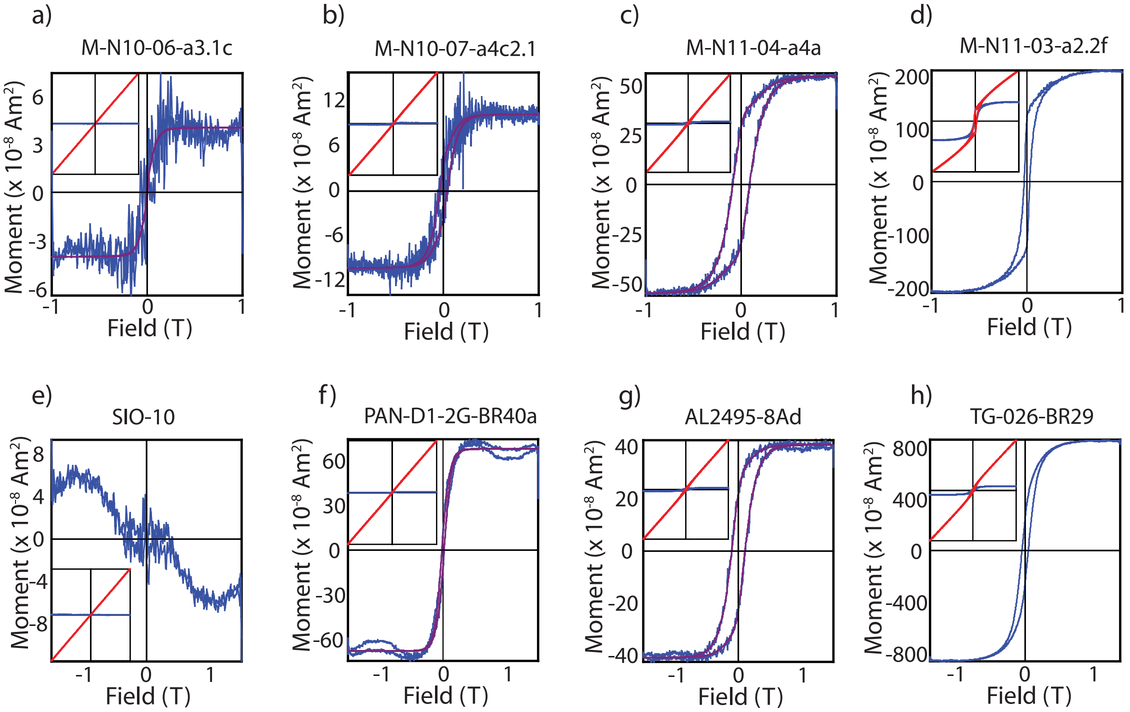

Figure 4. Example hysteresis data. (a–d) Synthetic samples. (e–h) Natural samples. Data from Figures 4a, 4e, and 4f were discarded. Inset shows raw data (red) and ferromagnetic loop (blue). Main frame shows same ferromagnetic loop (derived as in text) and (in some cases) a fit to the data using a set of hyperbolic basis functions (red).

the crucible) had a considerably stronger ferromagnetic-to-paramagnetic ratio (Figure 4d). In a few cases where a ferromagnetic signal was clearly defined, though noisy, data were fit with a series of hyperbolic basis functions (e.g., Figures 4b, 4c, and 4g), and hysteresis parameters were derived from this fit [*Jackson and Solheid*, 2010]. A ferromagnetic signal, though present, was extremely noisy and a reasonable fit was not achieved (e.g., Figures 4a and 4e) in 20 out of 23 group A (center) specimens, 14 out of 21 group B specimens, and 6 out of 52 group C (edge) specimens; hysteresis parameters are therefore not presented for these specimens.

[21] Many samples displayed nonlinear behavior in the high-field region ($B > 0.7$ T), and hysteresis parameters were thus calculated using an approach to saturation fit [*Jackson and Solheid*, 2010]. In spite of this, a number of specimens have values of saturation remanence to saturation magnetization (M_r/M_s) > 0.5 (Figure 5), the theoretical maximum predicted for assemblages of SD grains controlled by uniaxial anisotropy. Higher field (5 T) hysteresis loops from two representative samples suggest that these elevated M_r/M_s values result from insufficient saturation in a 1 T field, as noted by *Fabian* [2006] for titanomagnetite.

[22] Correlations between hysteresis parameters and experimental variables are strongest with respect to cooling rate (Figure 5a). The general pattern is consistent with rapidly cooled samples bearing a mixture of single-domain (SD) and superparamagnetic (SP) grains, while more slowly cooled samples are dominated by SD grains. Data from natural SBG overlap with the rapidly cooled samples (Figure 5), and show no trend with respect to age. Similar to the synthetic samples, most natural samples were dominated by a paramagnetic signal to the exclusion of an interpretable ferromagnetic signal and are not shown in Figure 5.

[23] The variability in crystallinity within each crucible is not fully characterized by the (necessarily) crude subdivision of specimens into groups A–C. We therefore represent finer variations in crystallinity by using the proxy $-\log_{10}(M_S)$. This proxy varies from ~0.5 (high crystallinity) to ~4.5 (low crystallinity), and hysteresis data are plotted as a function of this proxy in Figure 5b. Group A specimens (glassy crucible centers) have an average index of 3.7; group B, 3.0; and group C, 2.1. Regardless of location in the crucible or cooling rate, specimens with low degrees of crystallinity have a high SP contribution, while specimens with higher

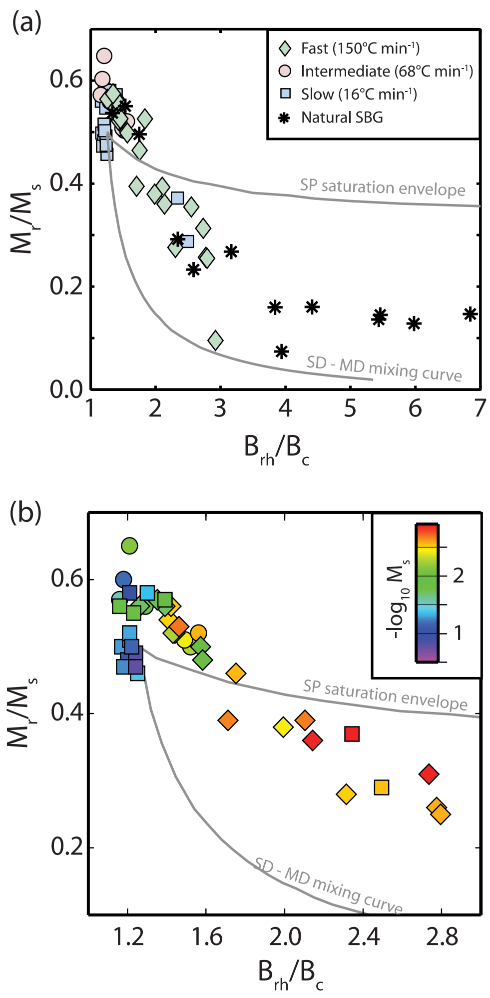

Figure 5. (a) Hysteresis parameters from sample splits not subjected to paleointensity experiments. Most are from splits adjacent to the crucible, as glassier samples had extremely high para- to ferromagnetic ratios. For reference, gray lines delineate the SP saturation envelope and an SD-MD mixing curve for magnetite from *Dunlop* [2002]. Elevated values for M_r/M_s (>0.5) likely result from insufficient saturation of the samples in a 1 T field (see text). The general pattern is consistent with rapidly cooled samples having a mixture of SD and SP grains, while more slowly cooled samples are predominantly SD data from natural SBG overlap with the quickly cooled samples. Note that one natural samples plots off scale at B_{rh}/B_c = 24.6, M_r/M_s = 0.06. (b) Expanded plot with only synthetic data. Color scaled to $-\log_{10}M_s$ as a proxy for degree of crystallinity. Purple (0.5) represents relatively high crystallinity and corresponds to samples that plot near the SD end-member. Red (3) represents relatively low crystallinity and corresponds to samples with a considerable SP contribution. Samples with even lower crystallinity have insufficient ferromagnetic contributions to properly determine hysteresis parameters. Symbol shape denotes cooling rate as in Figure 5a.

degrees of crystallinity plot near the SD end-member.

4.2.3. Unblocking and Ordering Temperatures (>300 K)

[24] Unblocking temperature (T_{ub}) data provide the strongest constraints on oxide composition in the absence of Curie temperature data. Specimens with a lower crystallinity index on average have more distributed unblocking temperatures with a higher maximum T_{ub} (as measured by the temperature

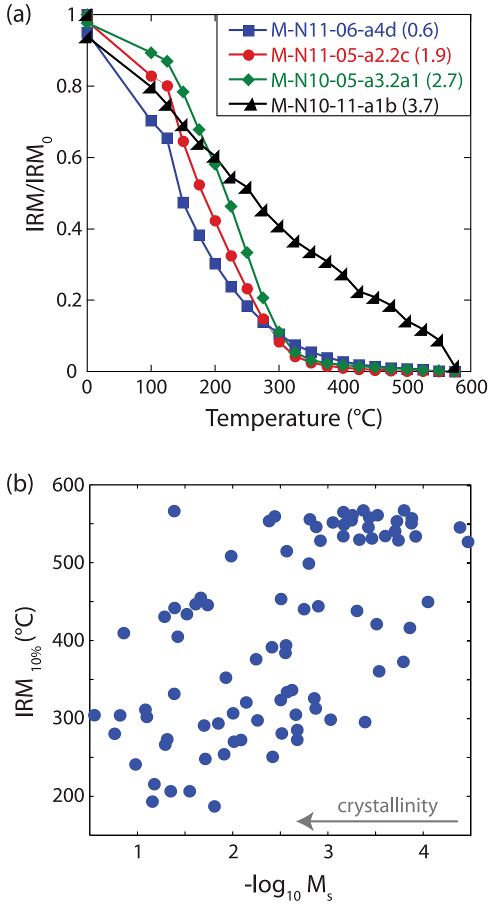

Figure 6. Thermal demagnetization of an IRM. (a) Example unblocking spectra demonstrate a progressive increase in unblocking temperatures with degree of crystallinity. Here $-\log_{10}M_s$ (as proxy for crystallinity) given in parentheses in legend; lower values correspond to higher degrees of crystallinity. Data shown are vector difference sums, but total moment data are nearly identical. (b) Temperature at which 10% of IRM remains (based on vector difference sum) plotted against the crystallinity proxy, $-\log_{10}M_s$. On average, samples with a higher degree of crystallinity have lower blocking temperatures than glassier samples. One specimen was not demagnetized to 10% of IRM by 575°C and is not shown.

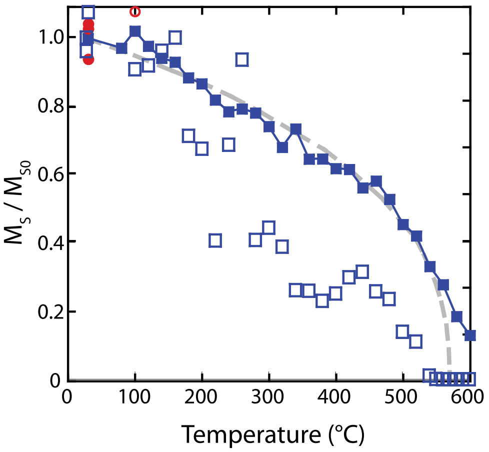

Figure 7. Saturation magnetization as a function of temperature derived from hysteresis loops. Solid symbols are specimen M-N10-07-a4c2.1 ($-\log_{10}M_s = 2.7$; Type C; Figure 4b). Open symbols are specimen M-N10-03-a2b4 $-\log_{10}M_s = 2.5$; Type C). Solid red circles show replicate room temperature measurements following heating to 420°C, 560°C, and 600°C for M-N10-07-a4c2.1 (no systematic change with temperature). Open red circles are replicate measurements at 100°C following heating to 400°C (off scale) and 600°C for M-N10-03-a2b4. Dashed gray line is M_s versus T for magnetite (data from B. Moskowitz, by *Banerjee* [1991]).

at which 10% of the IRM remains) than specimens with a higher index (Figure 6). More crystalline specimens typically unblock at <300°C (consistent with a relatively high Ti/Fe ratio). The distributed unblocking temperature spectra for glassy specimens is similar to that observed in natural SBG [e.g., *Pick and Tauxe*, 1993b; *Mejia et al.*, 1996; *Carlut and Kent*, 2000; *Bowles et al.*, 2006], remanence unblocks gradually between 100°C and $T_{ub\text{-}max}$ (usually ~400°C–580°C).

[25] This distributed unblocking could result from grain-size variations in compositionally homogoneous, stoichiometric magnetite near the SD-SP critical volume, as T_{ub} is proportional to grain volume. It could also result from varying Ti content in titanomagnetite grains of constant size. *Zhou et al.* [2000] observed that the composition of titanomagnetite grains becomes more variable with a lower average Ti content within 2–3 cm of the rim of a submarine basalt pillow. *Bowles et al.* [2006] noted that median destructive temperature of a large suite of SBG is inversely correlated with the Ti/Fe ratio of the bulk glass. These two observations suggest that composition plays a role. However, *Zhou et al.* [2000] also noted that samples from a young pillow's glassy, outer 2–3 cm have Curie temperatures as high as 580°C, suggesting nearly pure magnetite. Studies of Cretaceous glass have also suggested the presence of nearly pure magnetite, based on Curie temperature measurements [*Pick and Tauxe*, 1994] or the presence of the magnetite Verwey transition [*Riisager et al.*, 2003; *Smirnov and Tarduno*, 2003].

[26] In an attempt to distinguish between size and compositional effects on unblocking, we measured M_s (derived from hysteresis measurements and insensitive to grain size) as a function of temperature for two specimens. Out of necessity, we could not choose the glassiest specimens (e.g., Figure 4a), but selected the specimen shown in Figure 4b and another similar specimen from a different sample. Results from specimen M-N10-07-a4c2.1 (Figure 7) are consistent with temperature variations in M_s for pure magnetite and suggest that, at least in this specimen, a low-Ti phase dominates the M_s signal; it is therefore possible that the distributed unblocking results largely from grain-size variations. However, we note (below) that the magnetite Verwey transition is not observed in any specimens (synthetic or natural) tested, although the transition could be suppressed by nonstoichiometry or by a small amount of Ti. Data from the second specimen were significantly more noisy, but the trend appears considerably different, suggesting a range in Ti content (Figure 7).

4.2.4. Low-Temperature Data (<300 K)

[27] Much of the low-temperature data is not diagnostic, so we only briefly summarize results here; data are provided in the auxiliary material. During low-temperature cycling of a room temperature IRM, remanence in most samples increases on cooling, ranging from 10 to 40%; in some cases, this increase peaks at ~150 K, while in others the increase continues to 10 K (Figure S1). In general, the magnetization increase is greater in specimens with a higher degree of crystallinity (in both synthetic and natural samples), consistent with a greater contribution from high-Ti titanomagnetite, for which M_s increases more rapidly on cooling compared to magnetite. A distinct magnetite Verwey transition is not present in any specimens measured, but two of four Cretaceous glass specimens have a transition at 35 K, consistent with the presence of pyrrhotite [*Rochette et al.*, 1990] (Figure S1). This may be magmatic, primary pyrrhotite [e.g., *Mathez*, 1976], or a result of hydrothermal weathering [e.g., *Haymon and Kastner*, 1986].

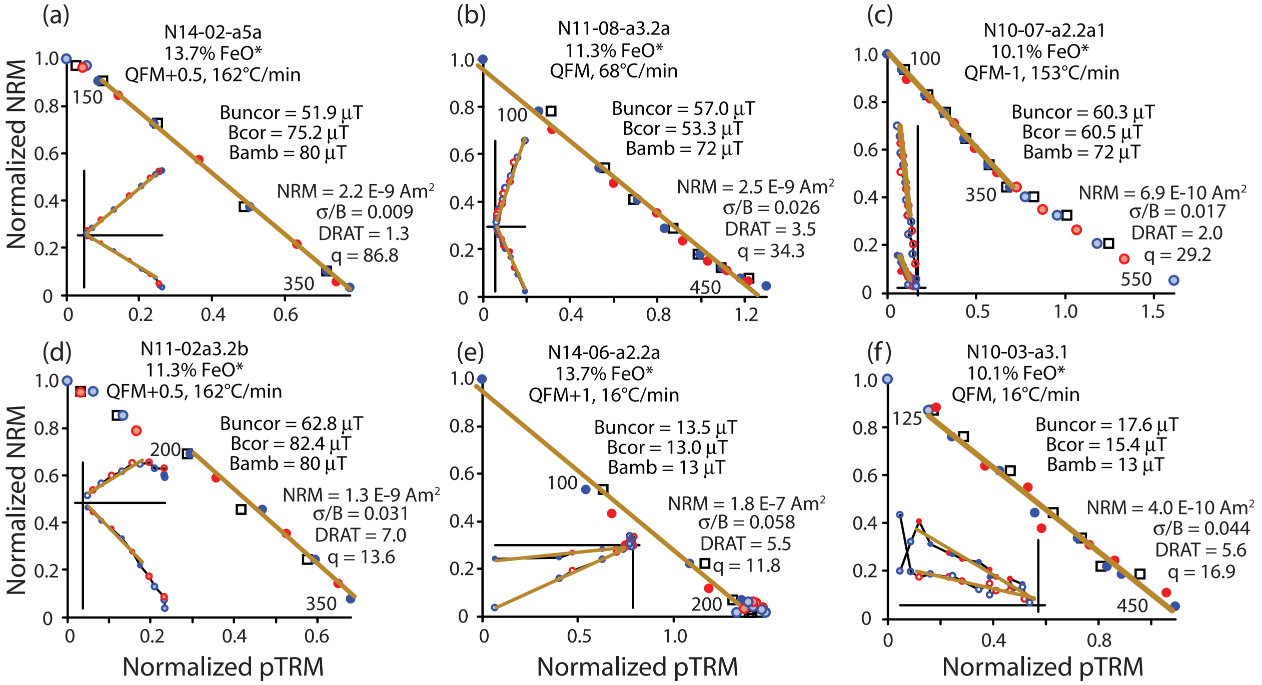

Figure 8. Representative paleointensity results for samples passing quality selection criteria. Blue circles indicate steps with zero-field heating followed by in-field heating (ZI). Red circles indicate steps with in-field heating followed by zero-field heating (IZ). Squares denote pTRM checks. Insets show vector endpoint diagrams of NRM data. B_{uncor} denotes raw paleointensity estimate, while B_{cor} is compensated for remanence anisotropy; B_{amb} is the approximate field in which samples were originally cooled.

4.3. Paleointensity Results

[28] Typical results of paleointensity experiments are shown in Figure 8, plotted as NRM remaining against partial TRM (pTRM) gained. Slopes representing paleointensity were selected for nearly all specimens in the following manner: the minimum temperature (T_{min}) was chosen to be the NRM unless a viscous remanent magnetization (VRM) with a direction different from the principal component could be identified. In the latter case, we selected the temperature at which the VRM was removed (typically 100°C to 150°C). The maximum temperature (T_{max}) was chosen to be that at which NRM ceased to be removed. In a few specimens, a sharp or subtle bend in the NRM-pTRM plot was present (e.g., Figure 8c), typically associated with increasing deviation of the pTRM checks at temperatures greater than the bend. In this case we selected T_{max} to be the temperature of this bend. Results of this exercise are shown in Table 3.

[29] Forty-one of 71 specimens are statistically anisotropic, with a mean maximum:minimum eigenvalue ratio of 1.6 (range 1.04–4.82) that is sufficient to significantly affect the remanence direction and intensity. A small number of specimens had weak moments and acquired little or no measurable TRM during the anisotropy experiment. With the exception of these specimens, we applied an anisotropy correction to all specimens (including those that were statistically isotropic, although here the correction is insignificant). The anisotropy correction decreased scatter that in some cases was large. For example, paleointensity estimates from sample M-N14-02 were distributed between 51 and 90 μT before anisotropy correction to 73–78 μT after correction. The anisotropy of TRM in many synthetic specimens likely arises from the preferred orientation of plagioclase nucleated on crucible walls. This in turn leads to distribution anisotropy [*Hargraves et al.*, 1991] in (titano)magnetite which crystallizes between the plagioclase crystals. This type of anisotropy is unlikely in natural SBG.

[30] In choosing a set of quality selection criteria, we examined the effect upon sample means of varying the cutoff value of a number of frequently used statistics. Much of the variation in sample means was controlled by scatter in the NRM-pTRM plot (e.g., Figures 7e and 7f), represented by the standard error of the slope divided by the slope $\sigma_b/|b|$ of *Coe et al.* [1978]. Many specimens with significant scatter had weak NRM moments (e.g.,

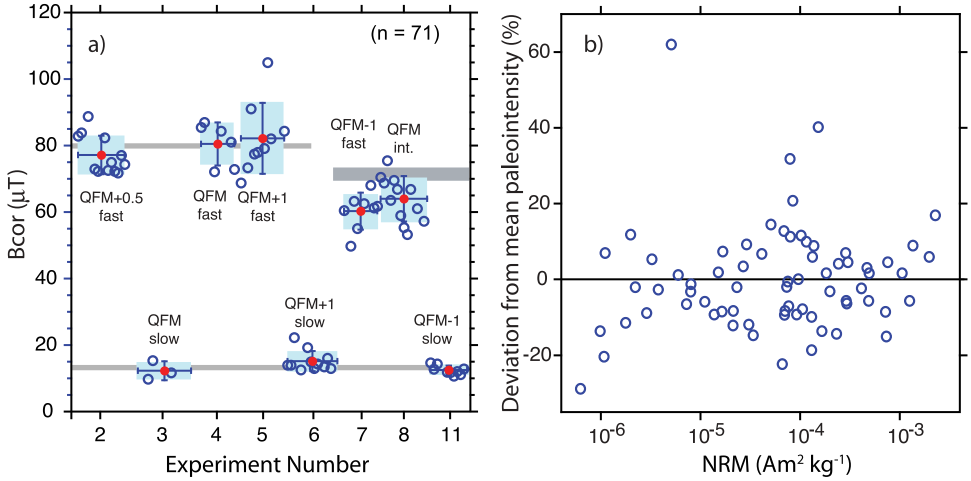

Figure 9. Summary of paleointensity results that passed quality selection criteria (see text). (a) Anisotropy-corrected experiment means. Each experiment is labeled with fO_2 and cooling rate and comprises results from three different bulk compositions. Small circles represent results from individual specimens. Red circle indicates the mean paleointensity, corrected for anisotropy (B_{cor}); blue box denotes 1σ error in Bcor. Horizontal gray bars indicate the laboratory field in which the glasses cooled. Results from syntheses cooled in 80 and 13 μT fields recover ambient laboratory field within error. Ambient field for remaining two experiments is less well determined and may be overestimated. (b) Percent deviation from mean paleointensity as a function of NRM. The absence of trend with respect to NRM implies that there are no systematic differences between glassy specimens and more crystalline specimens. Three paleointensity means were used: one for experiments 2, 4, and 5, one for 7 and 9, and one for 3, 6, and 11.

$<10^{-9}$ Am^2), which is also a frequent problem with natural SBG. Others had easily measurable moments and the nature of the resulting scatter is perplexing. We required all specimens to have $\sigma_b/|b| \leq 0.06$. As an additional check against thermochemical alteration, we required that the difference between repeat in-field steps normalized by the length of the selected NRM-pTRM segment [*Selkin and Tauxe*, 2000] be <7%. The application of these two selection criteria reduced the total number of specimens from 120 to 75. Prior to the first heating, NRM was measured twice; the second measurement followed storage in a magnetically shielded room for 36 h. An additional 5 specimens were rejected due to excessive (>20%) viscous decay. We combined all specimens synthesized in a single experiment to calculate average paleofield values (Figure 9a); this includes specimens from three different crucibles (samples) representing the three different compositions, which all should have experienced the same field. Samples cooled in the center of the furnace box (position A; Figure 1) recovered the measured field (13 μT) within error. The same is true for the first three experiments cooled outside the furnace box (position B; Figure 1), which agree with the field measured prior to the experiments (80 μT). The remaining two experiments (experiments 7 and 8) deviate significantly from the field measured prior to (80 μT) and after (~72 μT) the experiments; however, there is good internal consistency between these samples (6 crucibles) which give a paleofield of ~62 μT. The only shared characteristic between these two experiments is their proximity in time; they were carried out sequentially, but had different cooling rate and fO_2 conditions. The only plausible explanation for why only these two experiments deviate from the measured field is an undetected change in the laboratory field. We conclude that the actual laboratory field was ~60–65 μT during these experiments.

[31] The individual specimens included in the experiment paleointensity averages have varying degrees of crystallinity and are dominated by a titanomagnetite with widely varying Ti content. To check that glassy and crystalline specimens do not give different answers, we calculated the deviation from the mean paleointensity for each specimen (Figure 9b). There is no correlation between this deviation and mass-normalized magnetization (as a proxy for degree of crystallinity). There is also no significant correlation between paleointensity and any of the experimental variables (cooling rate, fO_2, or FeO*).

4.4. IRM Reheating Results

[32] IRM acquisition was measured following repeated heating (section 2.2) to test for the possible growth of magnetic phases. Results for these

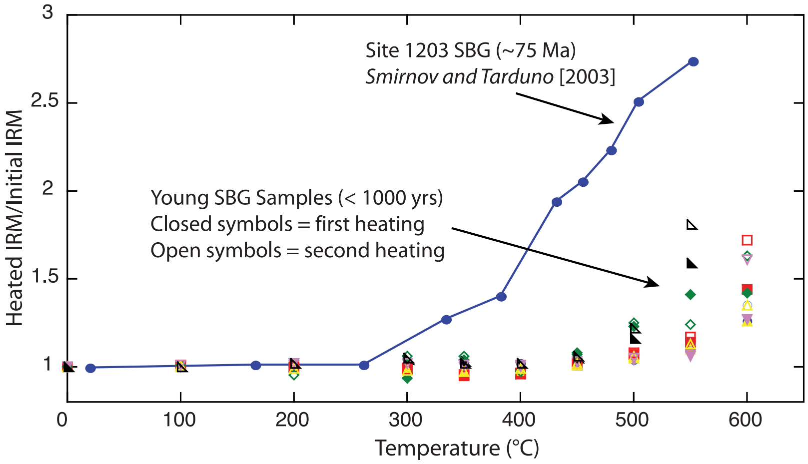

Figure 10. Variation in isothermal remanent magnetization (IRM) in glass samples subjected to stepwise heating. Colored symbols represent 6 young (<1 kyr) SBG samples that were progressively heated (twice to each temperature for 1 h). Young samples have little detectable magnetite production at temperatures < 400°C–450°C. Line shows results from an older (~75 Ma) SBG sample [*Smirnov and Tarduno*, 2003]. Note black triangles plot off scale at 600°C.

young (<1 ka), natural SBG have no increase in IRM acquisition below 400°C–450°C (Figure 10). Similar data from Cretaceous SBG [*Smirnov and Tarduno*, 2003] are shown for comparison.

5. Discussion

5.1. Relevance to Natural SBG

[33] Our synthetic samples were cooled in air and are thus not perfectly analogous to SBG, which is quenched in seawater. Quenching of natural SBG in seawater dominantly serves to increase cooling rate compared to subaerial eruptions, and because of the small thermal mass of our samples, we achieve similar rates in air. There is little evidence that natural SBG has incorporated significant seawater into the melt on quenching. Chlorine in fresh SBG provides a sensitive tracer for seawater or brine interaction. Low chlorine content (<150 ppm expected for fractionated melts) is interpreted as direct evidence for negligible interaction with seawater [e.g., *Michael and Schilling*, 1989; *Heide et al.*, 2008]. Higher chlorine contents (reaching several 1000 ppm) have been attributed to assimilation of altered crustal material or extremely chlorine-rich brines [*Michael and Schilling*, 1989; *Kent et al.*, 2002] in shallow magma chambers and not to direct interaction with seawater during quenching. Increased water content in fresh volcanic glass is linked to increased oxidation state of the melt [e.g., *Kelley and Cottrell*, 2009], but mid-ocean ridge basalt glasses have a narrow range of both fO_2 (0.41 ± 0.43 $\log_{10}$ units below QFM) [*Bezos and Humler*, 2005] and water (0.12–0.49 wt %) [e.g., *Danyushevsky et al.*, 2000; *Heide et al.*, 2008; *Kelley and Cottrell*, 2009]. These small variations are thought to reflect variations in mantle source or melting conditions.

[34] A small number of recent studies have questioned the extent to which seawater interacts with flows during emplacement. In certain types of lava flows, vaporized seawater may collect in cavities beneath the chilled margin of a flow, leading to crystallization of exotic phases (including Fe oxides and Fe sulfates) on the underside of this chilled surface [e.g., *Perfit et al.*, 2003; *Soule et al.*, 2006] that are absent on the outer chilled margin. Additionally, small bubbles of vaporized seawater may occasionally be incorporated into the outer glassy zone as the lava surface folds over onto itself, but there is no evidence for chemical interaction with the melt in this zone [*Soule et al.*, 2006].

[35] These observations suggest that the primary signature of quenching in seawater is rapid cooling, rather than chemical exchange. Although we cannot conclusively eliminate water as a factor contributing to magnetite formation in SBG, our experiments demonstrate that reasonable variations in fO_2 play little role in affecting magnetic properties, beyond influencing the concentration of oxide minerals. We have demonstrated that water (or any other external factor) is not required to generate a magnetic assemblage nearly identical to that observed in SBG.

5.2. Origin of Magnetism

[36] Hysteresis and unblocking temperature data are consistent with a fine-grained, low-Ti magne-

tite phase, similar to that observed in natural SBG, forming during initial quench of the synthetic samples. Only if crystallization is allowed to proceed (as happened near crucible margins) does a high-Ti phase develop and dominate the magnetic signature. In contrast to speculations by *Heller et al.* [2002], it is clear that the low-Ti magnetite is a primary, not secondary, phase. Results from a companion study [*Burgess et al.*, 2010] further demonstrate that the magnetic properties of this phase do not significantly alter with reheating (in air) at temperatures below the glass transition temperature (T_g). Although indirect, the data strongly suggest that the low-Ti phase forms predominantly at $T > T_g$ (680°C), which is well above the magnetite Curie temperature (580°C).

[37] The exact mechanism by which low-Ti magnetite forms in the quenched glass remains unclear. *Zhou et al.* [2000] suggested that the observed trends in titanomagnetite Ti content in a basalt pillow (equilibrium composition in the center and more scattered values with an average approaching the melt in the rapidly cooled margins) result from a strong kinetic effect on the mobility of cations in the melt. This phenomenon has been experimentally observed for plagioclase [*Lofgren*, 1980] and in other silicate systems [*Roskosz et al.*, 2005, 2006]. Furthermore, *Zhou et al.* [2000] proposed that the low Ti/Fe ratio (i.e., nearly pure magnetite) in the outermost glassy zone is controlled predominantly by diffusion processes, whereby the quickly grown and quenched magnetites preferentially incorporate elements with higher diffusivity (i.e., Fe over Ti).

[38] A second possibility, explored by *Burgess et al.* [2010], is (metastable) amorphous phase separation, which could explain both the lower average Ti content and the increased compositional heterogeneity observed by *Zhou et al.* [2000] near the pillow rim. In this scenario, a fine-scale (tens of nanometers) amorphous phase separation develops through spinodal decomposition during quenching. This process leads to some heterogeneity in the Ti/Fe ratio of the melt, and hence some heterogeneity in the Ti/Fe content of the nucleated oxides. The heterogeneity in Fe content is supported by low-temperature magnetic measurements on both synthetic and natural glass specimens that demonstrate rapid unblocking (on warming) of a SP phase at ~4 K [*Burgess et al.*, 2010]. *Hayashi et al.* [1999] noted a similar feature in synthetic silicate glass and suggested that it is associated with clusters of Fe atoms.

5.3. Implications for Paleointensity

[39] One of the most important criteria for recovering absolute paleointensity is that the sample carries a TRM. The results presented here, combined with the reheating experiments of *Burgess et al.* [2010], strongly suggest that the low-Ti magnetite is formed at $T > T_g > T_c$, and the glass should carry a total TRM. A fair question remains as to how this TRM-carrying phase may or may not be modified with time and temperature. Is the magnetic mineralogy stable during the experimental heating required in paleointensity experiments? Is it stable over geologic time as the glass undergoes relaxation and devitrification?

[40] Work by *Burkhard* [2001] on basaltic glass from Kilauea demonstrates growth of Fe-Ti oxides on reheating in air at temperatures >~850°C. The reheating experiments of *Burgess et al.* [2010] demonstrate that bulk magnetic properties undergo little to no change with heating at $T < T_g$ for times ranging from 7 months at 100°C to 100 h at 600°C. By contrast, specimens reheated at $T > T_g$ undergo dramatic changes in magnetization, magnetic grain size, and oxide composition. However, reheating experiments were all done on separate specimens, and there are no "before" data for those specific specimens that might allow us to evaluate subtle changes in magnetic properties. Heating of the two specimens shown in Figure 7 to 600°C in flowing He gas does result in an increase in remanence and development of a subtle magnetite Verwey transition that was not present prior to heating.

[41] Additionally, the glass transition temperature may be more properly thought of as a temperature interval (±100°C in width) over which the structural relaxation time undergoes a dramatic increase on cooling. Both time and temperature can lead to structural relaxation of the glass, and as a sample spends extended periods of time (hours) at elevated temperatures, T_g will decrease, possibly leading to induced crystallization at reduced (<680°C) temperatures. We note that a number of observations appear to support this interpretation. Thermomagnetic (M_s versus T) curves for Cretaceous glass are reversible up to 600°C [*Pick and Tauxe*, 1993a], suggesting that when heating and cooling are relatively rapid (5–10°C min^{-1}) the growth of magnetic phases is suppressed. IRM acquisition following heating at time scales relevant to paleointensity experiments shows no increase below 400°C–450°C (Figure 10), again suggesting that any low-temperature production of magnetite will be slow, limited by the long structural relaxation times at these

temperatures. This experiment is consistent with observations from many Thellier-type experiments on natural SBG, including the present study; pTRM checks rarely reveal any significant alteration below 400°C, but occasionally begin to deviate significantly at higher temperatures. Similar experiments by *Smirnov and Tarduno* [2003] (Figure 10) and [*Riisager et al.*, 2003] on Cretaceous glasses show more significant alteration beginning at lower temperatures (~300°C). This is consistent with a reduction in T_g as the glass relaxes over 75–120 Ma, and newly acquired T_g data demonstrate that two Cretaceous glass specimens have $T_g = \sim300°C$. By contrast, young (<40 ka) SBG have glass transitions > 650°C [*Bowles et al.*, 2005], and two 200 ka specimens have $T_g = 605°C$.

6. Conclusions

[42] We carried out an experimental examination of the timing and temperature of low-titanium magnetite formation in basaltic glass. Our primary conclusions are as follows.

[43] 1. The low-Ti magnetite is a primary phase, formed during rapid quenching of the glass. Only if crystallization of the glass is allowed to proceed does a high-Ti, equilibrium phase develop and dominate the magnetic signature.

[44] 2. Paleointensity experiments on synthetic samples all recover the known field, within 1σ error. The two exceptions are experiments that give field values internally consistent within and between experiments, suggesting that the actual field was somewhat lower than expected. This is consistent with a change in the ambient laboratory field near the end of the sample syntheses.

[45] 3. Young SBG (less than at least 200 ka) is entirely suitable for paleointensity studies. Older glass, however, is more likely to alter during laboratory experiments, and it may be possible that only the lowest blocking temperatures may be used for paleointensity estimates.

Acknowledgments

[46] The authors thank Pat Castillo for providing some of the basalt used as experimental starting materials and Peter Solheid for helping to set up the gas-mixing furnace. JB benefited from several very interesting discussions about rock magnetism with Mike Jackson and Bruce Moskowitz. Thanks to Andrew Roberts, Yongjae Yu, and one anonymous reviewer whose comments helped improve the paper. This work was supported by National Science Foundation grant EAR-0537981 to JSG and EAR-0538170 to RFC. The Institute for Rock Magnetism (IRM) is supported by the Instrumentation and Facilities Program of the National Science Foundation, Earth Science Division, and by the University of Minnesota. This is IRM contribution 1004.

References

Alt, J. C., and P. Mata (2000), On the role of microbes in the alteration of submarine basaltic glass: A TEM study, *Earth Planet. Sci. Lett.*, *181*, 301–313, doi:10.1016/S0012-821X(00)00204-1.

Banerjee, S. K. (1991), Magnetic properties of Fe-Ti oxides, in *Oxide Minerals: Petrologic and Magnetic Significance*, *Rev. Mineral.*, vol. 25, edited by D. H. Lindsley, pp. 107–128, Mineral. Soc. of Am., Washington, D. C.

Banerjee, N., and K. Muehlenbachs (2003), Tuff life: Bioalteration in volcaniclastic rocks from the Ontong Java Plateau, *Geochem. Geophys. Geosyst.*, *4*(4), 1037, doi:10.1029/2002GC000470.

Bergmanis, E., J. Sinton, K. Rubin, J. J. Mahoney, J. Bowles, J. S. Gee, and M. C. Smith (2004), Magma reservoir dynamics and diverse mantle melting at the Southern East Pacific Rise: 17°22′S–17°35′S, *Eos Trans. AGU*, *85*(47), Fall Meet. Suppl., Abstract V53A-0611.

Bezos, A., and E. Humler (2005), The $Fe^{3+}/\Sigma Fe$ ratios of MORB glasses and their implications for mantle melting, *Geochim. Cosmochim. Acta*, *69*, 711–725, doi:10.1016/j.gca.2004.07.026.

Bowles, J., J. Gee, D. V. Kent, E. Bergmanis, and J. M. Sinton (2005), Cooling rate effects on paleointensity estimates in submarine basaltic glass and implications for dating young flows, *Geochem. Geophys. Geosyst.*, *6*, Q07002, doi:10.1029/2004GC000900.

Bowles, J., J. S. Gee, D. Kent, M. Perfit, S. Soule, and D. Fornari (2006), Paleointensity applications to timing and extent of eruptive activity, 9°–10°N East Pacific Rise, *Geochem. Geophys. Geosyst.*, *7*, Q06006, doi:10.1029/2005GC001141.

Buddington, A. F., and A. F. Lindsley (1964), Iron-titanium oxide minerals and synthetic equivalent, *J. Petrol.*, *5*, 310–357.

Burgess, K., R. F. Cooper, J. A. Bowles, J. S. Gee, and D. J. Cherniak (2010), Effects of open and closed system oxidation on texture and magnetic response of remelted basaltic glass, *Geochem. Geophys. Geosyst.*, *11*, Q10007, doi:10.1029/2010GC003248.

Burkhard, D. J. M. (2001), Crystallization and oxidation of Kilauea basalt glass: Processes during reheating experiments, *J. Petrol.*, *42*, 507–527, doi:10.1093/petrology/42.3.507.

Carlut, J., and D. V. Kent (2000), Paleointensity record in zero-age submarine basalt glasses: Testing a new dating technique for recent MORBs, *Earth Planet. Sci. Lett.*, *183*, 389–401, doi:10.1016/S0012-821X(00)00291-0.

Carlut, J., X. Quidelleur, V. Courtillot, and G. Boudon (2000), Paleomagnetic directions and K/Ar dating of 0 to 1 Ma lava flows from La Guadeloupe Island (French West Indies): Implications for time-averaged field models, *J. Geophys. Res.*, *105*, 835–849, doi:10.1029/1999JB900238.

Carlut, J., M. H. Cormier, D. V. Kent, K. E. Donnelly, and C. H. Langmuir (2004), Timing of volcanism along the northern East Pacific Rise based on paleointensity experiments on basaltic glasses, *J. Geophys. Res.*, *109*, B04104, doi:10.1029/2003JB002672.

Coe, R. S. (1967), The determination of paleo-intensities of the earth's magnetic field with emphasis on mechanisms which could cause non-ideal behavior in Thellier's method, *J. Geomagn. Geoelectr.*, *19*, 157–179.

Coe, R. S., S. Grommé, and E. A. Mankinen (1978), Geomagnetic paleointensities from radiocarbon-dated lava flows on Hawaii and the question of the Pacific nondipole low, *J. Geophys. Res.*, *83*, 1740–1756, doi:10.1029/JB083iB04p01740.

Cooper, R. F., W. Yoon, and J. Perepezko (1991), Internal nucleation of highly undercooled magnesium metasilicate melts, *J. Am. Ceram. Soc.*, *74*, 1312–1319, doi:10.1111/j.1151-2916.1991.tb04104.x.

Danyushevsky, L. V., S. M. Eggins, T. J. Falloon, and D. M. Christie (2000), H_2O abundance in depleted to moderately enriched mid-ocean ridge magmas; Part I: Incompatible behavior, implications for mantle storage, and origin of regional variations, *J. Petrol.*, *41*, 1329–1364, doi:10.1093/petrology/41.8.1329.

Dunlop, D. J. (2002), Theory and application of the Day plot (M_{rs}/M_s versus H_{cr}/H_c): 1. Theoretical curves and tests using titanomagnetite data, *J. Geophys. Res.*, *107*(B3), 2056, doi:10.1029/2001JB000486.

Fabian, K. (2006), Approach to saturation analysis of hysteresis measurements in rock magnetism and evidence for stress dominated magnetic anisotropy in young mid-ocean ridge basalt, *Phys. Earth Planet. Inter.*, *154*, 299–307, doi:10.1016/j.pepi.2005.06.016.

Gee, J. S., S. C. Cande, J. A. Hildebrand, K. Donnelly, and R. L. Parker (2000), Geomagnetic intensity variations over the past 780 kyr obtained from near-seafloor magnetic anomalies, *Nature*, *408*, 827–832, doi:10.1038/35048513.

Ghiorso, M. S., and R. O. Sack (1995), Chemical mass-transfer in magmatic processes IV. A revised and internally consistent thermodynamic model for the interpolation and extrapolation of liquid-solid equilibria in magmatic systems at elevated temperatures and pressures, *Contrib. Mineral. Petrol.*, *119*, 197–212, doi:10.1007/BF00307281.

Goguitchaichvili, A., L. M. Alva-Valdivia, J. Rosas-Elguera, J. Urrutia-Fucugauchi, and J. Sole (2004), Absolute geomagnetic paleointensity after the Cretaceous Normal Superchron and just prior to the Cretaceous-Tertiary transition, *J. Geophys. Res.*, *109*, B01105, doi:10.1029/2003JB002477.

Hargraves, R. B., D. Johnson, and C. Y. Chan (1991), Distribution anisotropy: The cause of AMS in igneous rocks?, *Geophys. Res. Lett.*, *18*, 2193–2196, doi:10.1029/91GL01777.

Hayashi, M., M. Susa, and K. Nagata (1999), Magnetic structure of as-quenched silicate glasses containing iron oxides, *J. Appl. Phys.*, *85*, 2257–2263, doi:10.1063/1.369535.

Haymon, R., and M. Kastner (1986), The formation of high-temperature clay-minerals from basalt alteration during hydrothermal discharge on the East Pacific Rise axis at 21°N, *Geochim. Cosmochim. Acta*, *50*, 1933–1939, doi:10.1016/0016-7037(86)90249-8.

Heide, K., E. Woermann, and G. Ulmer (2008), Volatiles in pillows of the Mid-Ocean-Ridge-Basalt (MORB) and vitreous basaltic rims, *Chem. Erde*, *68*, 353–368, doi:10.1016/j.chemer.2008.07.001.

Heller, R., R. T. Merrill, and P. L. McFadden (2002), The variation of intensity of Earth's magnetic field with time, *Phys. Earth Planet. Inter.*, *131*, 237–249, doi:10.1016/S0031-9201(02)00038-9.

Hort, M., and T. Spohn (1991), Crystallization calculations for a binary melt cooling at constant rates of heat removal: Implications for the crystallization of magma bodies, *Earth Planet. Sci. Lett.*, *107*, 463–474, doi:10.1016/0012-821X(91)90093-W.

Jackson, M., and P. Solheid (2010), On the quantitative analysis and evaluation of magnetic hysteresis data, *Geochem. Geophys. Geosyst.*, *11*, Q04Z15, doi:10.1029/2009GC002932.

Kelley, K. A., and E. Cottrell (2009), Water and the oxidation state of subduction zone magmas, *Science*, *325*, 605–607, doi:10.1126/science.1174156.

Kent, A. J. R., D. W. Peate, S. Newman, E. M. Stolper, and J. A. Pearce (2002), Chlorine in submarine glasses from the Lau Basin: seawater contamination and constraints on the composition of slab-derived fluids, *Earth Planet. Sci. Lett.*, *202*, 361–377, doi:10.1016/S0012-821X(02)00786-0.

Kirkpatrick, R. J. (1978), Processes of crystallization in pillow basalts, Hole 396B, DSDP Leg 46, *Initial Rep. Deep Sea Drill. Proj.*, *46*, 271–282.

Kirschvink, J. L. (1980), The least-squares line and plane and the analysis of palaeomagnetic data, *Geophys. J. R. Astron. Soc.*, *62*, 699–718.

Kruber, C., I. H. Thorseth, and R. B. Pedersen (2008), Seafloor alteration of basaltic glass: Textures, geochemistry, and endolithic microorganisms, *Geochem. Geophys. Geosyst.*, *9*, Q12002, doi:10.1029/2008GC002119.

Lofgren, G. (1971), Experimentally produced devitrification textures in natural rhyolitic glass, *Geol. Soc. Am. Bull.*, *82*, 111–124, doi:10.1130/0016-7606(1971)82[111:EPDTIN]2.0.CO;2.

Lofgren, G. (1980), Experimental studies on the dynamic crystalization of silicate melts, in *Physics of Magmatic Processes*, edited by R. B. Hargraves, pp. 487–551, Princeton Univ. Press, Princeton, N. J.

Marescotti, P., D. A. Vanko, and R. Cabella (2000), From oxidizing to reducing alteration: Mineralogical variations in pillow basalts from the east flank, Juan de Fuca Ridge, *Proc. Ocean Drill. Program Sci. Results*, *168*, 119–136.

Mathez, E. (1976), Sulfur solubility and magmatic sulfides in submarine basalt glass, *J. Geophys. Res.*, *81*, 4269–4276, doi:10.1029/JB081i023p04269.

Mejia, V., N. D. Opdyke, and M. R. Perfit (1996), Paleomagnetic field intensity recorded in submarine basaltic glass from the East Pacific Rise, the last 69 ka, *Geophys. Res. Lett.*, *23*, 475–478, doi:10.1029/96GL00018.

Michael, P. J., and J.-G. Schilling (1989), Chlorine in mid-ocean ridge magmas: Evidence for assimilation of seawater-influenced components, *Geochim. Cosmochim. Acta*, *53*, 3131–3143, doi:10.1016/0016-7037(89)90094-X.

Morales, J., A. Goguitchaichvili, E. Canon-Tapia, and R. Negrete (2003), Further absolute geomagnetic paleointensities from Baja California: Evaluation of Pliocene and Early/Middle Pleistocene data, *C. R. Geosci.*, *335*, 995–1004, doi:10.1016/j.crte.2003.07.002.

Muhe, R., and P. Stoffers (1995), Rock structures and mineral assemblage associated with hydroexpansion in mid-oceanic ridge basalts, *Mineral. Petrol.*, *54*, 71–83, doi:10.1007/BF01162759.

Perfit, M. R., J. R. Cann, D. J. Fornari, J. Engels, D. K. Smith, W. I. Ridley, and M. H. Edwards (2003), Interaction of sea water and lava during submarine eruptions at mid-ocean ridges, *Nature*, *426*, 62–65, doi:10.1038/nature02032.

Pick, T., and L. Tauxe (1993a), Geomagnetic palaeointensities during the Cretaceous normal superchron measured using submarine basaltic glass, *Nature*, *366*, 238–242, doi:10.1038/366238a0.

Pick, T., and L. Tauxe (1993b), Holocene paleointensities: Thellier experiments on submarine basaltic glass from the

East Pacific Rise, *J. Geophys. Res.*, *98*, 17,949–17,964, doi:10.1029/93JB01160.

Pick, T., and L. Tauxe (1994), Characteristics of magnetite in submarine basaltic glass, *Geophys. J. Int.*, *119*, 116–128, doi:10.1111/j.1365-246X.1994.tb00917.x.

Riisager, P., J. Riisager, X. Zhao, and R. S. Coe (2003), Cretaceous geomagnetic paleointensities: Thellier experiments on pillow lavas and submarine basaltic glass from the Ontong Java Plateau, *Geochem. Geophys. Geosyst.*, *4*(12), 8803, doi:10.1029/2003GC000611.

Rochette, P., G. Fillion, J. Mattei, and M. Dekkers (1990), Magnetic transition at 30–34 K in pyrrhotite—Insight into a widespread occurrence of this mineral in rocks, *Earth Planet. Sci. Lett.*, *98*, 319–328, doi:10.1016/0012-821X(90)90034-U.

Roskosz, M., M. J. Toplis, P. Besson, and P. Richet (2005), Nucleation mechanisms: A crystal-chemical investigation of phases forming in highly supercooled aluminosilicate liquids, *J. Non-Cryst. Solids*, *351*, 1266–1282, doi:10.1016/j.jnoncrysol.2005.02.021.

Roskosz, M., M. Toplis, and P. Richet (2006), Kinetic vs. thermodynamic control of crystal nucleation and growth in molten silicates, *J. Non Cryst. Solids*, *352*, 180–184, doi:10.1016/j.jnoncrysol.2005.11.009.

Rubin, K., M. C. Smith, E. Bergmanis, M. R. Perfit, J. M. Sinton, and R. Batiza (2001), Geochemical heterogeneity within mid-ocean ridge lava flows: Insights into eruption, emplacement and global variations in magma generation, *Earth Planet. Sci. Lett.*, *188*, 349–367, doi:10.1016/S0012-821X(01)00339-9.

Selkin, P., and L. Tauxe (2000), Long-term variations in palaeointensity, *Philos. Trans. R. Soc. London A*, *358*, 1065–1088, doi:10.1098/rsta.2000.0574.

Smirnov, A. V., and J. A. Tarduno (2003), Magnetic hysteresis monitoring of Cretaceous submarine basaltic glass during Thellier paleointensity experiments: Evidence for alteration and attendant low field bias, *Earth Planet. Sci. Lett.*, *206*, 571–585, doi:10.1016/S0012-821X(02)01123-8.

Soule, S. A., D. J. Fornari, M. R. Perfit, W. I. Ridley, M. H. Reed, and J. R. Cann (2006), Incorporation of seawater into mid-ocean ridge lava flows during emplacement, *Earth Planet. Sci. Lett.*, *252*, 289–307, doi:10.1016/j.epsl.2006.09.043.

Staudigel, H., H. Furnes, N. Mcloughlin, N. Banerjee, L. Connel, and A. Templeton (2008), 3.5 billion years of glass bioalteration: Volcanic rocks as a basis for microbial life?, *Earth Sci. Rev.*, *89*, 156–176, doi:10.1016/j.earscirev.2008.04.005.

Storrie-Lombardi, M. C., and M. R. Fisk (2004), Elemental abundance distributions in suboceanic basalt glass: Evidence of biogenic alteration, *Geochem. Geophys. Geosyst.*, *5*, Q10005, doi:10.1029/2004GC000755.

Stroncik, N., and H. Schmincke (2001), Evolution of palagonite: Crystallization, chemical changes, and element budget, *Geochem. Geophys. Geosyst.*, *2*(7), 1017, doi:10.1029/2000GC000102.

Tauxe, L. (2006), Long-term trends in paleointensity: The contribution of DSDP/ODP submarine basaltic glass collections, *Phys. Earth Planet. Inter.*, *156*, 223–241, doi:10.1016/j.pepi.2005.03.022.

Tauxe, L., and H. Staudigel (2004), Strength of the geomagnetic field in the Cretaceous Normal Superchron: New data from submarine basaltic glass of the Troodos Ophiolite, *Geochem. Geophys. Geosyst.*, *5*, Q02H06, doi:10.1029/2003GC000635.

Thellier, E., and O. Thellier (1959), Sur l'intensité du champ magnétique terrestre dans le passé historique et géologique, *Ann. Geophys.*, *15*, 285–378.

Thorseth, I., T. Torsvik, V. Torsvik, F. Daae, and R. Pedersen (2001), Diversity of life in ocean floor basalt, *Earth Planet. Sci. Lett.*, *194*, 31–37, doi:10.1016/S0012-821X(01)00537-4.

Yu, Y., and L. Tauxe (2005), Testing the IZZI protocol of geomagnetic field intensity determination, *Geochem. Geophys. Geosyst.*, *6*, Q05H17, doi:10.1029/2004GC000840.

Yu, Y., L. Tauxe, and A. S. Genevey (2004), Toward an optimal geomagnetic field intensity determination technique, *Geochem. Geophys. Geosyst.*, *5*, Q02H07, doi:10.1029/2003GC000630.

Zhou, W., R. Van der Voo, D. R. Peacor, and Y. Zhang (2000), Variable Ti-content and grain size of titanomagnetite as a function of cooling rate in very young MORB, *Earth Planet. Sci. Lett.*, *179*, 9–20, doi:10.1016/S0012-821X(00)00100-X.

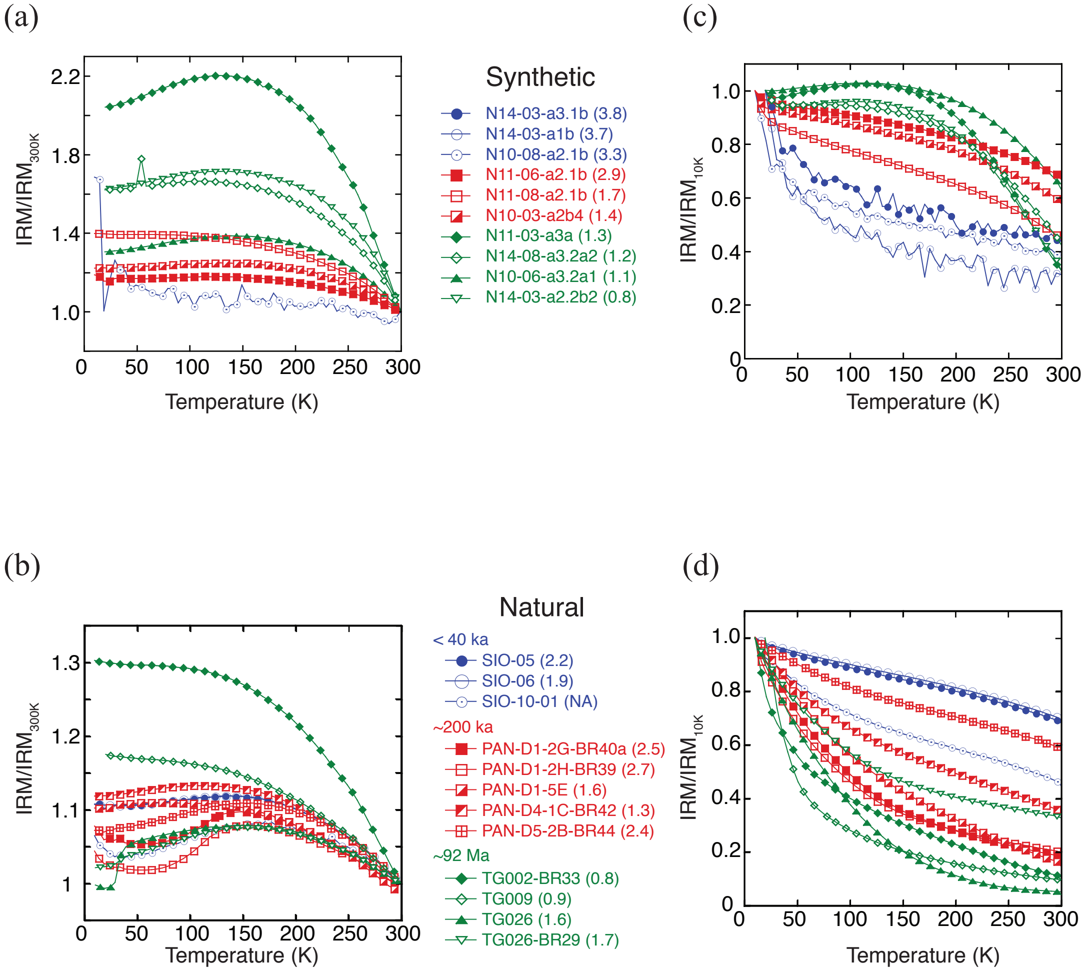

Auxiliary Figure 1. Low-temperature (10-300K) magnetic data. A 2.5 T IRM was imparted at 300K (RTSIRM), and remanence was measured on cooling in synthetic **(a)** and natural **(b)** samples. Following zero-field cooling (ZFC) from 300K to 10 K, a 2.5 T IRM was imparted at 10 K, and remanence was measured on warming in synthetic **(c)** and natural **(d)** samples. Crystallinity proxy ($-\log_{10}M_s$) is given in parentheses following specimen ID. Smaller values correspond to higher degrees of crystallinity.

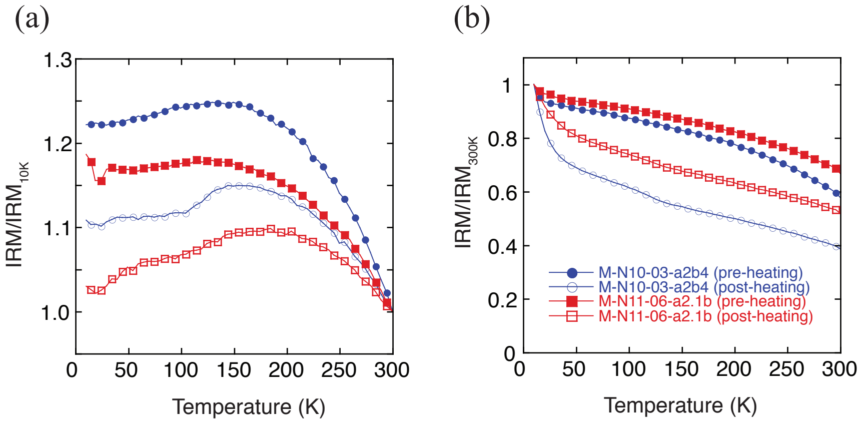

Auxiliary Figure 2. 300 K IRM (RTSIRM) measured on cooling (a) and 10 K IRM (ZFC) measured on warming (b) for two synthetic samples before (closed symbols) and after (open symbols) heating to 600°C. Note the development of a subtle magnetite Verwey transition at ~120 K post-heating.